



1 **Investigation of the climatology of low-level jets over North**  
2 **America in a high-resolution WRF simulation**

3

4 Xiao Ma<sup>1,2</sup>, Yanping Li<sup>1,2</sup>, Zhenhua Li<sup>1</sup>, Fei Huo<sup>1</sup>

5 <sup>1</sup>Global Institute for Water Security, University of Saskatchewan, 11 Innovation Blvd, Saskatoon, SK, S7N 3H5,  
6 Canada

7 <sup>2</sup>School of Environment and Sustainability, University of Saskatchewan, 117 Science Place, Saskatoon, SK, S7N 5C8,  
8 Canada

9 *Correspondence to:* Yanping Li (yanping.li@usask.ca)

10 **Abstract.** In this study, we utilized a high-resolution (4 km) convection-permitting Weather Research Forecasting  
11 (WRF) simulation spanning a 13-year period (2000-2013) to investigate the climatological features of Low-level Jets  
12 (LLJs) over North America. The 4-km simulation enabled us to represent the effects of orography and the underlying  
13 surface on the boundary layer winds better. Focusing on the continental US and the adjacent border regions of Canada  
14 and Mexico, this study characterizes the spatial distribution, seasonal patterns, and diurnal fluctuations of  
15 northerly/southerly LLJ occurrence frequencies. This paper not only identified several well-known large-scale LLJs  
16 in North America, such as the southerly Great Plains LLJ and the summer northerly California coastal LLJ, but also  
17 the Quebec northerly LLJ, which gets less focus before. Moreover, the high-resolution simulation revealed climatic  
18 characteristics of weaker and smaller-scale LLJs or low-level wind maxima in regions with complex terrains, such as  
19 the northerly LLJs in the foothill regions of the Rocky Mountains and the Appalachian during the winter. Additionally,  
20 the different thermal and dynamic mechanisms forming significant LLJs near the Great Plains, California, and Quebec  
21 are investigated. This study provides valuable insights into the climatological features of LLJs in North America and  
22 the high-resolution simulation offers a more detailed understanding of LLJ behavior near complex terrains and other  
23 smaller-scale features.

24



## 25 1. Introduction

26 A low-level jet (LLJ) is generally described as the fast-moving air ribbon located in the lower atmosphere (Bonner,  
27 1968; Rife et al., 2010). Many of the world's LLJs have been studied, such as the Great Plains LLJ over the central  
28 US (Bonner, 1968; Zhong et al., 1996), the Somali LLJ over eastern Africa (Munday et al., 2021), and the South  
29 American LLJ over the east Andes Mountains (Montini et al., 2019). A kind of mesoscale weather system, an LLJ has  
30 a relatively small vertical range of usually only a few hundred meters, but its width can reach several hundred  
31 kilometers. LLJs are closely related to precipitation and even extreme events, and they can transfer abundant water  
32 vapor to the downwind regions, providing favorable dynamic conditions for rainfall (Walters and Winkler, 2001;  
33 Hodges and Pu, 2019). Because LLJs also affect processes such as wind power development, air pollution  
34 transportation, and urban heat islands (Hu et al., 2013; Sullivan et al. 2017; Gadde and Stevens 2021, Ma et al., 2022),  
35 researchers have long been interested in investigating their features.

36 Since the mid-20th century, scientists have used regular rawinsonde observations to investigate the characteristics of  
37 LLJs. Applying rawinsondes to investigate the Great Plains LLJ in the central US, Bonner (1968), Mitchell et al.  
38 (1995), and Walters et al. (2008) studied its distribution, seasonal activity, horizontal and vertical structure, and diurnal  
39 features and established the climatology of the Great Plains LLJ during warm seasons. As well as rawinsondes, radar  
40 systems and wind profilers are useful tools for characterizing LLJs. Frisch et al. (1992) observed a typical LLJ process  
41 using Doppler weather radar in North Dakota and identified that the friction on the surface of the boundary layer is  
42 important in the early stages of LLJ development. Using long-term wind profiler measurement, Miao et al. (2018)  
43 interpreted the climatology of LLJs in Beijing and Guangzhou, concluding that the frequency values of LLJs in these  
44 two cities are 13.0% and 4.9%, respectively. Moreover, Smith et al. (2019) used the Plains Elevated Convection at  
45 Night (PECAN) observations to conduct high-quality measurements of nocturnal LLJs with wide spatial and temporal  
46 resolutions. They found that sudden changes in LLJ structure typically result from the spatial evolution of the LLJ.

47 However, there are some disadvantages of observational research that should be noted. First, regular rawinsonde data  
48 only contain measurements at two daily time points (00 UTC and 12 UTC), which cannot fully capture LLJs' diurnal  
49 variations. The density of observations is therefore coarse, and coastal areas lack regular high-density measurements,  
50 making the study of coastal LLJs challenging (Mitchell et al., 1995). Second, heterogeneities in the rawinsonde records,  
51 such as variations in station locations, radiosonde types, and archiving procedures, may also complicate the use of



52 these observations in climate research. Third, rawinsonde measurements taken at a single point are not able to capture  
53 horizontal shear and environmental conditions (Chen et al., 2005). Although observations platforms such as radar or  
54 field projects like PECAN can compensate to some extent for this lack of observational data, these approaches are still  
55 limited by the spatial coverage of their measurement platforms (Smith et al., 2019).

56 Because of these problems with observational methods, researchers have chosen reanalysis datasets as an alternative  
57 for investigating LLJs. Reanalysis data have relatively better spatial and temporal coverage than rawinsonde  
58 measurements, incorporate observations into the preliminary model simulations, perform more extensive  
59 measurements, and contain broader domains. Rife et al. (2010) highlighted the global distribution of identified  
60 nocturnal LLJs using reanalysis data with a horizontal grid spacing of 40 km, and even successfully extracted some  
61 previously unknown jets. Doubler et al. (2015) applied the North American Regional Reanalysis (NARR) dataset (~32  
62 km) to generate long-term LLJ climatology in North America. Consistent with previous records, Doubler's results  
63 supplemented the description of some smaller-scale LLJs. Similarly, Montini et al. (2019) compared and validated the  
64 performance of five different reanalysis datasets in identifying LLJs. Their results showed the 38-year climatology of  
65 South American LLJs with ERA-Interim data (~79 km).

66 Scientists have also conducted studies based on numerical simulations, which can more accurately represent LLJs than  
67 reanalysis data sets, especially in the vertical direction, thereby yielding new insights into LLJs' features. Tang et al.  
68 (2017) used an ensemble of dynamically downscaling regional climate simulations to generate the climatology of  
69 Great Plains LLJ and predicted that the LLJ will occur more frequently during the nighttime in spring and summer in  
70 mid-21st century. Jiménez-Sánchez et al. (2019) conducted a simulation for LLJs over the Orinoco River Basin by  
71 dynamic downscaling of the Weather Research and Forecasting model (WRF). The simulation represented the jet  
72 streaks better than previous studies within a broader region of wind enhancement and illustrated more detailed diurnal  
73 evolution. Nevertheless, most general numerical simulations still represent the convective processes by the  
74 parameterization scheme, which generates uncertainty in the results. These issues can be addressed by using  
75 convection-permitting models with grid spacing under 5 km that adequately simulate the convections and other small-  
76 scale processes (Liu et al., 2017, Li et al., 2019, Kurkute et al., 2020). Convection-permitting modeling describes the  
77 underlying surface more accurately than coarse-resolution simulations and reanalysis data and shows promise in  
78 investigations of LLJs near complex mountain areas. Du and Chen (2019) analyzed the LLJs over southern China by



79 using 4-km WRF model and revealed a solid relationship between the mesoscale lifting of LLJs and the convection's  
80 initiation. They also highlighted the importance of coastal terrain. Overall, the finer-resolution tools tend to show more  
81 comprehensive and precise results, offering detailed and accurate references to LLJs.

82 The formation mechanisms of LLJs have been studied extensively by researchers. In the inertial oscillation theory  
83 proposed by Blackadar (1957) and Stensrud (1996), it is suggested that the diurnal cycle feature of the Great Plains  
84 LLJ is related to the friction change in the boundary layer. During the night, the jet-core wind is enhanced after  
85 decoupling with near-surface friction. Holton (1967) and Parish (2000) developed the thermal wind adjustment theory,  
86 which suggests that the horizontal pressure gradient changes because the atmosphere over sloping terrain is warmer  
87 or because sea-land contrast influences the diurnal cycle of wind. Additionally, LLJs can also be formed due to  
88 synoptic system forcing, as proposed by Uccellini et al. (1987) and Saulo et al. (2007). However, convection-  
89 permitting models can help explain how LLJs form because they have precise descriptions of weather systems and  
90 underlying orography. Using 4-km simulations, Fu et al. (2018) and Zhang et al. (2019) analyzed the evolution of  
91 LLJs over mountainous areas in eastern and southwestern China, respectively. They concluded that inertial oscillation  
92 plays a prominent role in and is responsible for the local precipitation peak at a certain time. Besides, Shapiro et al.  
93 (2016) argued that the formation of some LLJs may not be impacted by a single factor and that a unified theory  
94 analysis is thus required. Thus, a dataset that offers more information must be very popular. All these studies have  
95 shown that convection-permitting models, with both finer coverage and resolutions, are a powerful tool for LLJ  
96 climatology research.

97 The purpose of this study is to use the 4-km convection-permitting WRF model (Liu et al., 2017) to produce a detailed  
98 LLJ climatology. This paper focuses on the features of LLJs in major areas of North America and aims to provide  
99 alternative dataset sources with the finer spatial and temporal resolution for the LLJs in this region and provide more  
100 helpful tools for LLJs-related studies in other disciplinary. Section 2 introduces the model configuration and the  
101 criteria for LLJ identification, Section 3 presents the characteristics of LLJ frequencies in North America, and Section  
102 4 illustrates the analysis of the background and mechanisms in several LLJ cases. Finally, Section 5 provides the  
103 discussion and conclusion.

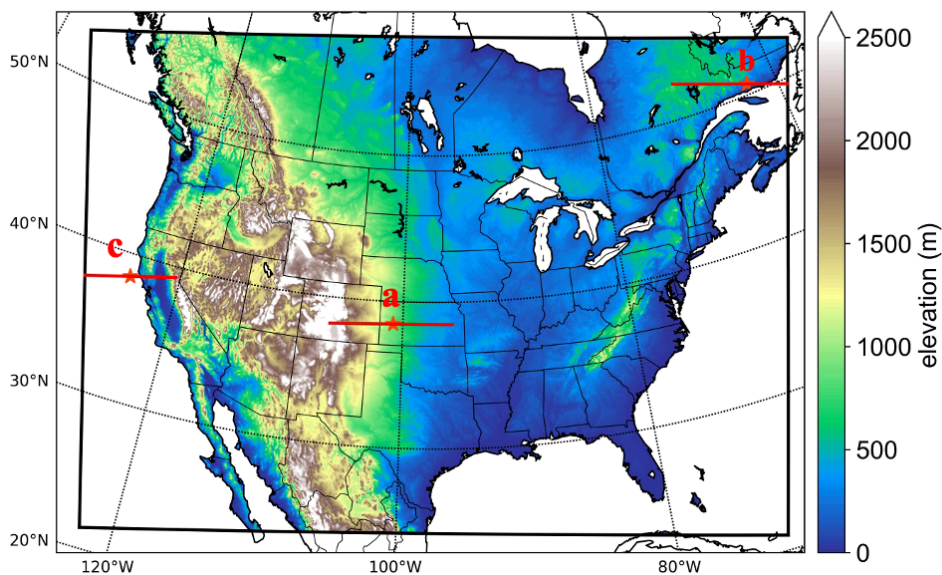




104 **2. Model configuration and methods**

105 **2.1 WRF setup**

106 This study utilized a convection-permitting Weather Research and Forecasting (WRF) dataset (Liu et al. 2017, Data  
107 available at: <https://rda.ucar.edu/datasets/ds612.0/>) with a horizontal resolution of 4 km over North America. The  
108 domain covers the entire continental US, Southern Canada, and Northern Mexico, as illustrated in Figure 1. The  
109 simulation provides three-dimensional data at a temporal resolution of 3 hours, resulting in 8-time steps per day. In  
110 the vertical direction, the data have 51 eta levels and can reach 50 hPa. And it should be noted that there are five layers  
111 under 500-m height and nine layers under 1 km are outputted above ground level, which means the WRF has the good  
112 ability to capture the LLJs occurring in the boundary layer. The simulation period spans from 1st October 2000 to  
113 30th September 2013, and the six-hourly ERA-Interim reanalysis dataset of 0.7° resolution was used as input for the  
114 climate simulation. The simulation did not apply any cumulus parameterization scheme due to the fine horizontal grid  
115 spacing, but other sub-grid scale processes were parameterized by various physical schemes: the rapid radiative  
116 transfer model (RRTMG) (Iacono et al., 2008) was used for simulating longwave and shortwave radiations, the Yonsei  
117 University (YSU) scheme was used for representing the planetary boundary layer (Hong et al., 2006), and the Noah-  
118 MP model was used for computing surface processes (Niu et al., 2011). In this study, the planetary boundary layer  
119 scheme is retained, but it should be noted that this would introduce uncertainties to the simulation in the vertical  
120 direction, especially in regions with complex topography.



121  
122 **Figure 1.** Study domain of this convection-permitting model. The colors represent the elevation. The red lines and stars  
123 show the positions of investigated cross-section and jets in Section 4.

124

## 125 **2.2 Methodology**

126 Using the threshold criteria proposed by Bonner (1968), this study identifies LLJs from the vertical wind profile of  
127 each grid point in the model output data. LLJs are present when the following conditions are met: (1) the height of the  
128 LLJ core maximum wind speed is below 3 km above the ground level (AGL); (2) the maximum wind speed is greater  
129 than or equal to 12 m s<sup>-1</sup>; (3) from the height of the wind maxima to the height of the next minimum value or 3-km  
130 height (whichever is lower), the velocity of winds drop by at least 6 m s<sup>-1</sup>; (4) the wind speed drops by at least 6 m s<sup>-1</sup>  
131 below the level of wind maxima. Considering the importance of the meridional LLJ for heat and water vapor  
132 transport, this study addresses their frequencies in different meridional directions. According to Walter et al. (2008)  
133 and Doubler et al. (2015), the criteria for identifying different meridional LLJs are as follows: for southerly LLJs (S-  
134 LLJs), the wind direction is between 113° and 247°; for northerly LLJs (N-LLJs), the direction is between 293° and  
135 67°. These criteria are used in this study.

136 Based on the identification criteria above, we determined if the LLJ existed at each grid point and consequently  
137 counted the occurrences of S-LLJs and N-LLJs. We also calculated the frequencies of LLJs in different seasons or



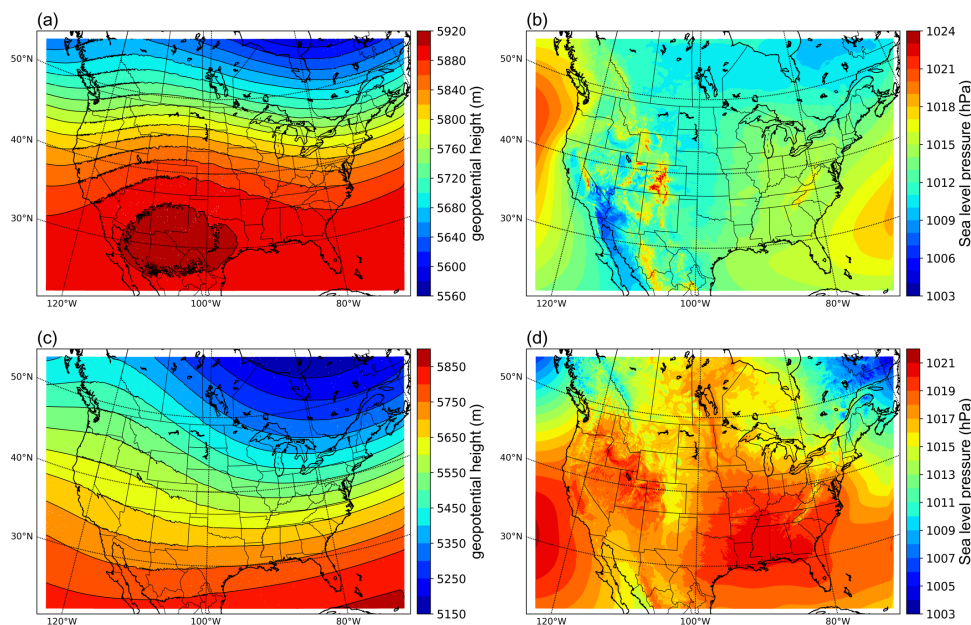
138 time steps. The frequency is defined as the percentage of the total number of occurrences for the selected accumulation  
139 period. We generated the frequency distribution maps for LLJs climatology in North America, which are illustrated  
140 in Section 3.

### 141 3. The climatology of North American LLJs

#### 142 3.1 Analysis of atmospheric circulation

143 This study adopts model data to capture the climatological features of LLJs in North America. Considering the  
144 relationship between LLJs and synoptical systems, we evaluated the ability of the convection-permitting model to  
145 simulate the background atmospheric circulation. Figure 2 depicts the simulated climatology of geopotential heights  
146 at 500 hPa and sea-level pressure isobars for summer and winter. In summer, at a height of 500 hPa (Figure 2a), In  
147 summer, the model depicts a trough in the east of the continental US, a ridge over the Rocky Mountains, and the  
148 upper-air subtropical anticyclone crossing the southern US. At sea level (Figure 2b), the model captures the Azores  
149 High-Pressure area in the Atlantic Ocean and the Hawaiian High-Pressure area in the Pacific.

150 In winter, the contours at the pressure value of 500 hPa (Figure 2c) show stronger fluctuating characteristics: the  
151 eastern trough and western ridge over the continent strengthen, and the polar vortex extends to the northern US, while  
152 most of North America is controlled by a cold high-pressure system. In addition, the subtropical anticyclone is too  
153 weak to be found within the study domain. On the other hand, most of North America is controlled by a cold high-  
154 pressure system at sea level (Figure 2d), and parts of the Icelandic Low and Aleutian Low appear on both east and  
155 west of Canada, even though their centers are not captured in the domain. To summarize, the convection-permitting  
156 model can simulate the features of semi-permanent centers of atmospheric circulations in North America, thus  
157 demonstrating its strength in identifying the LLJs in this area.



158

159 **Figure 2. Climatology of atmospheric circulations simulated by the convection-permitting model: (a) summer 500 hPa**  
160 **geopotential height; (b) sea-level pressure in summer; (c)-(d) the same variables but in winter.**

161

## 162 3.2 Seasonal variations of LLJs

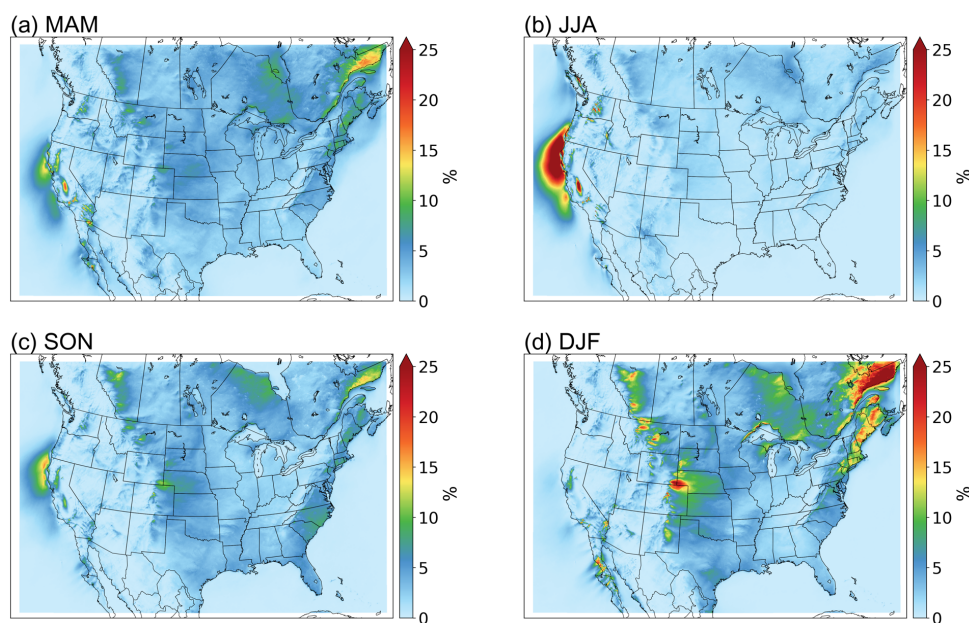
### 163 3.2.1 Northerly LLJs

164 Figure 3 shows the frequency distribution of N-LLJ in four seasons, in which the frequency represents the ratio  
165 between the seasonal total number of LLJs occurrence and the total time steps in each season. Clearly, the California  
166 coastal LLJ is strongest in summer (June, July, and August (JJA)), with a large area of N-LLJ frequency greater than  
167 25%, extending from the southern Oregon coast to the central California coast. Regions with a frequency greater than  
168 5% can even extend to the Pacific Ocean near northern Baja California. However, from summer to autumn (September,  
169 October, and November (SON)), the frequency of this LLJ decreases sharply, with a frequency of only 5%-15% in  
170 the core region, and it is only distributed on the northern coast of California. In winter (Dec, Jan, and Feb (DJF)) it  
171 occurs very infrequently (~3%).

172 On the other hand, various N-LLJ phenomena occur frequently in the cold season. These N-LLJs are mainly located  
173 near the eastern slopes of special terrains such as the Rocky Mountains, Appalachian Mountains, and the Quebec



174 Labrador Plateau. In winter, high frequencies ( $>10\%$ ) are observed from western Alberta to Oklahoma, within which  
175 hot spots are distributed sporadically in Alberta, Montana, Wyoming, and Colorado. These hot spots have frequencies  
176 of about 20%, especially in the region between Colorado and Wyoming. In over 25% of the wind profiles, the N-LLJs  
177 can even be extracted. The N-LLJs over the Eastern US coast mainly extend from Maine to South Carolina, and their  
178 highest frequency can reach about 15%-20%. The N-LLJs in eastern Quebec also occur most frequently in winter  
179 ( $>25\%$ ). Over Hudson Bay, the simulation can also detect the N-LLJ from about 10% of the time steps. The  
180 frequencies of all the N-LLJs mentioned above decline significantly in spring, and it is hard to detect them in summer  
181 as the frequencies are mostly less than 5%.



182  
183 **Figure 3. Seasonal occurrence frequency of N-LLJs. Frequency shown here is calculated by counting the number of**  
184 **occurrences of LLJs in each three-hourly time step and then dividing the total number of LLJs in each season by the number**  
185 **of time steps in that season.**

### 186 3.2.2 Southerly LLJs

187 As to the climatology of S-LLJs in different seasons (see Figure 4), in winter, in the broad region extending from the  
188 south Texas-west Gulf of Mexico to southern Iowa, the frequencies of S-LLJs exceed 10%. The greatest frequencies  
189 of S-LLJs ( $>20\%$ ) are found along the border between northeastern Mexico and the United States. In addition, about



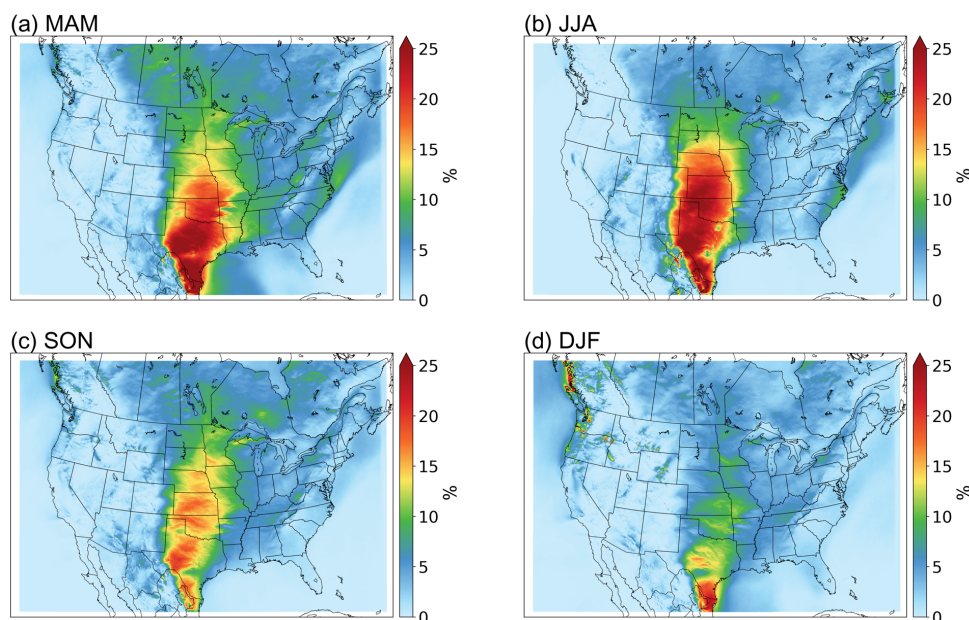
190 15% of the simulated wind profiles in south-central Texas are identified as S-LLJs. In the spring (March, April, and  
191 May), the frequency expands significantly in >10% of areas, with clear S-LLJ distributions detected in Manitoba,  
192 Saskatchewan, and other parts of Canada. The highest frequencies are still found in the Texas-Mexico area, where the  
193 magnitude of these frequencies increases to over 25%. This region also extends northward to occupy most of Texas.  
194 In winter, S-LLJs with occurrence frequencies of above 15% extend to near Colorado and Nebraska.

195 In summer, the area with frequencies greater than 10% no longer extends to the central Canadian prairie provinces  
196 and Tennessee. The S-LLJs over the western Gulf of Mexico are also difficult to identify with modeled data, and their  
197 frequency is close to 0%. In contrast, the area with frequencies exceeding 25% extends northward in summer and is  
198 roughly divided into three parts distributed respectively in the northeast Mexico-Texas border, west-central Texas,  
199 and the central US Great Plains (western Oklahoma and southern Kansas). The regions where more than 15% of the  
200 wind profiles are identified as S-LLJ also expand from Colorado to near South Dakota.

201 In the fall, the magnitude of the frequency of S-LLJs decreases dramatically in the central US Plains and Texas. The  
202 frequency still maintains a level greater than 15% in most areas, but with a maximum frequency of only 20% and  
203 sporadically located in southwest Texas. The frequencies greater than 10% again expand northward and eastward in  
204 this season, reaching Manitoba and Ontario.

205 There are also several S-LLJs on a smaller scale that can be seen on the seasonal S-LLJ climatology map. In spring, a  
206 narrow region of S-LLJs with a frequency greater than 5% on the eastern side of the Appalachians extends from  
207 Georgia through the western Atlantic to southern Nova Scotia. Over the Atlantic near eastern Maryland, the frequency  
208 of the S-LLJ can exceed 10%. In summer, this narrow frequency belt still exists and has the same coverage, but the  
209 magnitude of the frequency decreases and the frequency >10% is no longer visible. In winter, a region where S-LLJ  
210 frequency is >5% extends from southwest Oregon to the west coast of British Columbia. But in spring, S-LLJs with  
211 frequencies >5% occur only over the ocean west of British Columbia. As for the summer, S-LLJs are almost  
212 undetectable in this region.





213

214 **Figure 4. Seasonal frequency of S-LLJs.**

215 To summarize, for the LLJ systems that have been investigated by many researchers, the convection-permitting WRF  
216 model performs well in observing the Great Plains S-LLJ and California coastal N-LLJ during the summer. But as to  
217 the winter LLJs that lack attention, it is essential to compare and validate the occurrence and features revealed by  
218 WRF simulation. Therefore, the ERA5 reanalysis dataset is applied in this study for capturing the LLJs in winter using  
219 the same criterion. Appendix after the text shows the results of the comparison between ERA5 and WRF simulation.

### 220 **3.3 Diurnal variations of LLJs**

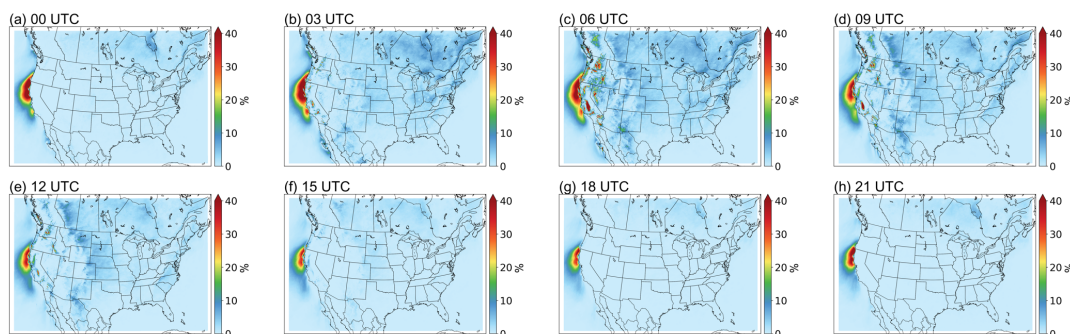
221 To show the diurnal features of the LLJs, we selected summer and winter as the representative seasons because LLJs  
222 occur most frequently in these seasons. Below, the descriptions are divided into N-LLJs and S-LLJs.

#### 223 **3.3.1 Northerly LLJs**

224 The California coastal N-LLJ is the most highlighted low-level jet system in this region in summer. As seen in Figure  
225 5, it occurs throughout the day over the eastern Pacific Ocean from Oregon to the California coast. Figure 5 also shows  
226 that the California Coastal N-LLJ has diurnal characteristics: from 21 UTC, the low-level jet begins to develop, with  
227 a N-LLJ frequency of >30%, expanding until it reaches its maximum at 03 UTC – 06 UTC. Then the high-frequency

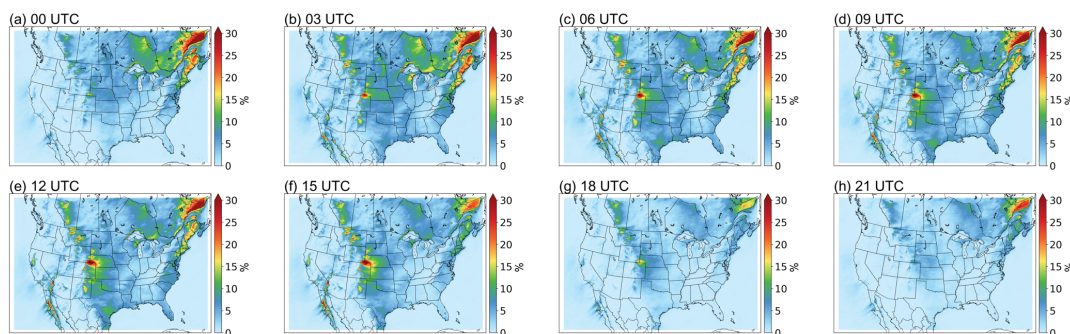


228 coverage of the California coastal LLJ gradually shrinks, reaching the minimum at 18 UTC and only existing off the  
229 northwest coast of California. At the same time, the N-LLJ over the Hudson Bay Plain is also at its maximum  
230 frequency (>5%) from 03 UTC – 06 UTC, but it rarely occurs at other time steps.



231  
232 **Figure 5. Diurnal frequency of N-LLJs in the summer (JJA).**

233 In winter (Figure 6), three types of N-LLJs over the Hudson Bay Plain, the eastern slopes of the Quebec Labrador  
234 Plateau, and the Appalachians display similar diurnal fluctuations. All three N-LLJs reach their highest frequency at  
235 03 UTC and their lowest at 18 UTC. The only difference among the three types is that the smallest frequency of the  
236 Quebec N-LLJ still endures at a level of greater than 15%, while the other two N-LLJs mostly have frequencies of  
237 about 5%. The smallest frequency (~5%) of N-LLJs occurs downstream of the Rocky Mountains (over Alberta,  
238 Montana, and Kansas) at 21 UTC. In the subsequent development stage, the changes in the sporadic hot spots  
239 distributed near the eastern boundary of the Rocky Mountains are more significant. As seen in Figure 6, frequency  
240 starts growing from 00 UTC and then peaks at 12 UTC, especially the wind maxima located in Colorado, Wyoming,  
241 and Kansas, where the highest frequency can be >25%.



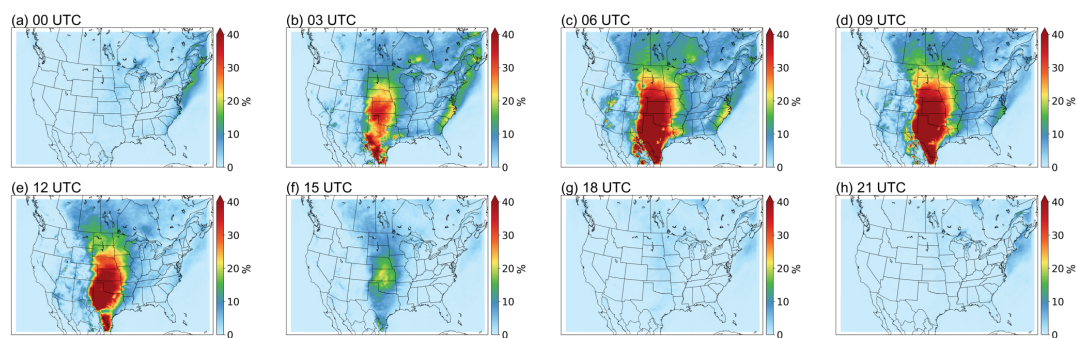
242  
243 **Figure 6. Diurnal frequency of N-LLJs in winter (DJF).**





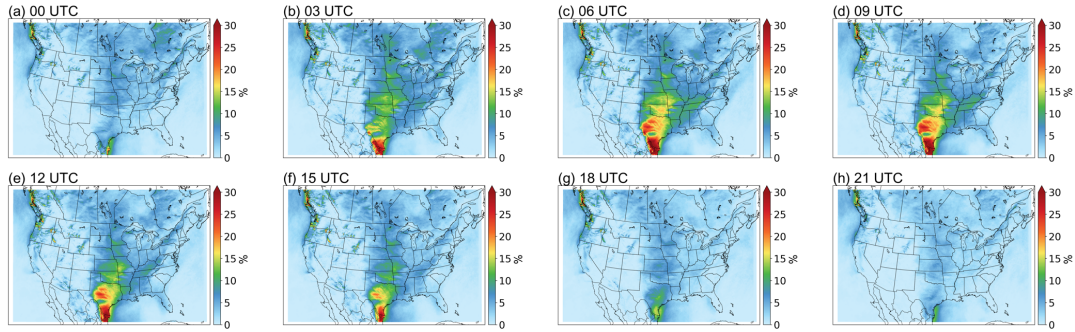
### 244 3.3.2 Southerly LLJs

245 In summer, the Great Plains S-LLJ occurs more frequently than in other seasons, and its diurnal variability is also the  
246 strongest in this season (see Figure 7). At noon local time and in the afternoon (18 UTC – 00 UTC), almost no S-LLJs  
247 occur over the central US (frequency <5% or about 0%). In contrast, the Great Plains LLJ begins to develop at 03  
248 UTC, when a frequency of over 25% extends from Mexico to Kansas. It reaches maximum strength at midnight (06  
249 UTC – 09 UTC), when the frequency reaches over 30% and the high-frequency coverage enlarges to the Dakotas, the  
250 border of the eastern Rocky Mountains, and western Minnesota, Missouri, and Louisiana. Summer S-LLJs are also  
251 active in southern Canada at night and in the early morning. In Saskatchewan, Manitoba, and central Ontario (03 UTC  
252 – 12 UTC, as shown in Figure 7), S-LLJs are found with frequency >15%. In the eastern US and Atlantic, S-LLJs  
253 occur most frequently at midnight (03 UTC – 06 UTC).



254  
255 **Figure 7. Diurnal frequency of S-LLJs in summer (JJA).**

256 For the cold season (Figure 8), even though the Great Plains LLJ is the most inactive based on the description in  
257 section 3.2, it still has a clear diurnal variation. Compared with the results in summer, the diurnal cycle of Great Plains  
258 LLJ in winter is not that significant: It mainly occurs over the western Gulf of Mexico and southern Texas, with the  
259 frequency in the afternoon (18 UTC – 21 UTC) declining to 5-10%. The S-LLJ develops from 03 UTC, gradually  
260 generating two high-frequency (20%-25%) centers in mid- and southeastern Texas at 06 UTC – 12 UTC. As for the  
261 S-LLJ near Vancouver Island, it is hard to see the diurnal variability: There is only a slight magnitude growth of  
262 frequency from the afternoon (00 UTC) to the evening (06 UTC), and the coverage is almost the same.



263

264 **Figure 8. Diurnal frequency of S-LLJs in winter (DJF).**

265

266 **4 Formation and evolution mechanisms of various LLJs**

267 Section 3's results illustrate the climatology of LLJs over North America, particularly their seasonal and diurnal  
 268 features. To explain the mechanisms, the inertial oscillation theory from Blackadar (1957) is used. Using this theory,  
 269 we start from the horizontal momentum equations and divide the actual horizontal wind  $u/v$  into two components—  
 270 geostrophic wind  $u_g/v_g$  and ageostrophic wind  $u_a/v_a$ :

271 
$$\frac{d(u_g + u_a)}{dt} = -\frac{1}{\rho} \frac{\partial P}{\partial x} + f(v_g + v_a) \quad (1.1)$$

272 
$$\frac{d(v_g + v_a)}{dt} = -\frac{1}{\rho} \frac{\partial P}{\partial y} - f(u_g + u_a) \quad (1.2)$$

273

274 In which  $\rho$  is air density,  $P$  is pressure, and  $f$  is the Coriolis parameter. Assuming the horizontal pressure gradient  
 275 is fixed, the geostrophic wind is a constant as well, which means  $\frac{du_g}{dt} = \frac{dv_g}{dt} = 0$ :

276 
$$\frac{du_a}{dt} = -\frac{1}{\rho} \frac{\partial P}{\partial x} + f(v_g + v_a) \quad (2.2)$$

277 
$$\frac{dv_a}{dt} = -\frac{1}{\rho} \frac{\partial P}{\partial y} - f(u_g + u_a) \quad (2.2)$$

278

279 When the definition of geostrophic wind  $u_g = -\frac{1}{\rho f} \frac{\partial P}{\partial y}$  and  $v_g = \frac{1}{\rho f} \frac{\partial P}{\partial x}$  is combined, the equation (2) is:

280 
$$\frac{du_a}{dt} = f v_a \quad (3.1)$$

281 
$$\frac{dv_a}{dt} = -f u_a \quad (3.2)$$

282



283 If  $\frac{d}{dt}$  is taken to both sides of the equations (3), then we get  $\frac{d^2 u_a}{dt^2} = -f^2 u_a$ , and  $\frac{d^2 v_a}{dt^2} = -f^2 v_a$ , thereby:

284 
$$u_a = c_1 \cos(ft) + c_2 \sin(ft) \quad (4.1)$$

285 
$$v_a = c_2 \cos(ft) - c_1 \sin(ft) \quad (4.2)$$

286

287 Therefore, according to the equations (4), the ageostrophic wind should theoretically have a circle-pattern variation  
288 and the vector must rotate clockwise with a period of  $2\pi/f$  (Blackadar, 1957; Van de Wiel et al., 2010). Under the  
289 condition of a constant geostrophic wind—when the ageostrophic vector rotates from the opposite to the same  
290 direction of geostrophic wind—the wind transitions from subgeostrophic to supergeostrophic. This change occurs  
291 because of decoupling with surface friction effects, then the wind gets unbalanced.

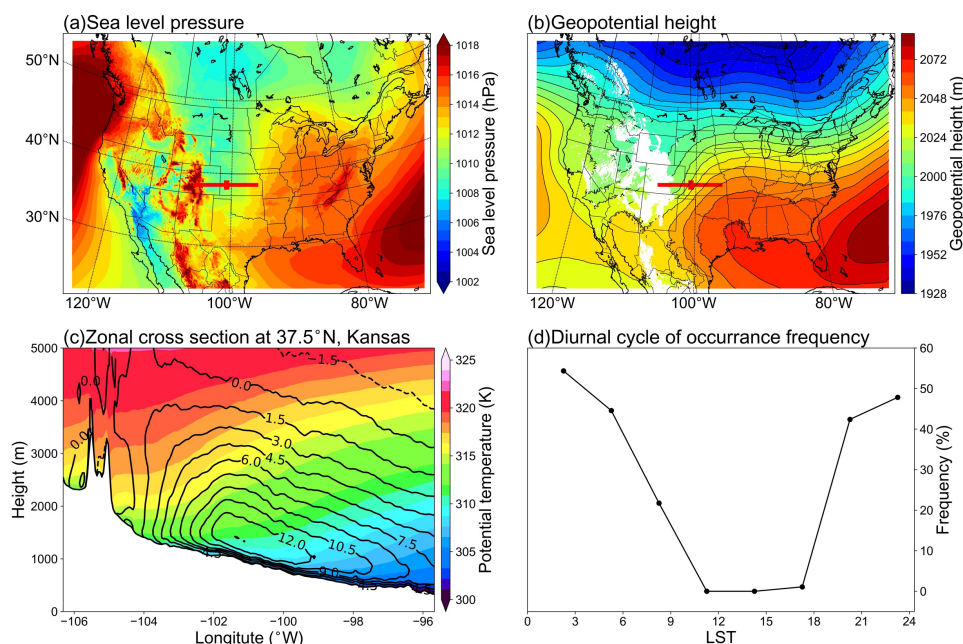
292 Other theories also help explain the formation of LLJs, such as the sloping-terrain thermodynamic mechanism (Holton,  
293 1967) and background synoptic system forcing (Uccellini et al., 1987). To understand the characteristics of the LLJs  
294 in this study, three typical cases are analyzed: Great Plains S-LLJ, Quebec N-LLJ, and California coastal N-LLJ. The  
295 locations for extracting data are shown in Figure 1 (solid lines and stars a, b, c).

#### 296 **4.1 Great Plains S-LLJ**

297 As Section 3's results show, the Great Plains S-LLJ typically occurs in summer and more frequently at night. To  
298 investigate its associated meteorological condition, this study extracts all the Great Plains S-LLJ cases occurs at the  
299 jet core in JJA. The jet core is defined by where the mean meridional wind is the strongest on the cross-section, and it  
300 locates at star A (shown in figure 1). The mean sea-level pressure and 800 hPa geopotential height are shown in Figure  
301 9a and 9b, respectively. The background large-scale circulations indicate that, at all the time points when the Great  
302 Plains S-LLJ occurs, the range of the subtropical anticyclone extends east of the Great Plains at both ground and low-  
303 level atmosphere. A high-pressure ridge is located near the gulf coast of Mexico and Texas (Figure 9b). Thus, clearly,  
304 the zonal pressure/geopotential gradient in the central US guides the dominant southerly winds around this region.  
305 The cross-section in Figure 9c illustrates a strong baroclinicity and shows that the isentropic line incline moves from  
306 east to west, as is typical for the sloping-terrain heating effect (Holton, 1967). This effect generates an upslope wind  
307 on the east side of the slope, and the airstream gradually turns northward due to the Coriolis force, creating the  
308 southerly LLJs. On the other hand, as can be seen in the frequency cycle in Figure 9d, at noon local time (at the



309 selected point-a in Figure 1), the frequency of the Great Plains LLJ is very low (close to 0%), rising to more than 40%  
310 after 18 LST even if the radiation is not at the day's peak.



311  
312 **Figure 9. Background circulations of the Great Plains S-LLJ: (a) sea-level pressure, (b) geopotential height of 800 hPa, (c)**  
313 **cross section including meridional winds (lines) and potential temperature (shading), and (d) diurnal cycle of frequency.**  
314 **The red lines and points in (a) and (b) show the position of cross-section and chosen jet core.**

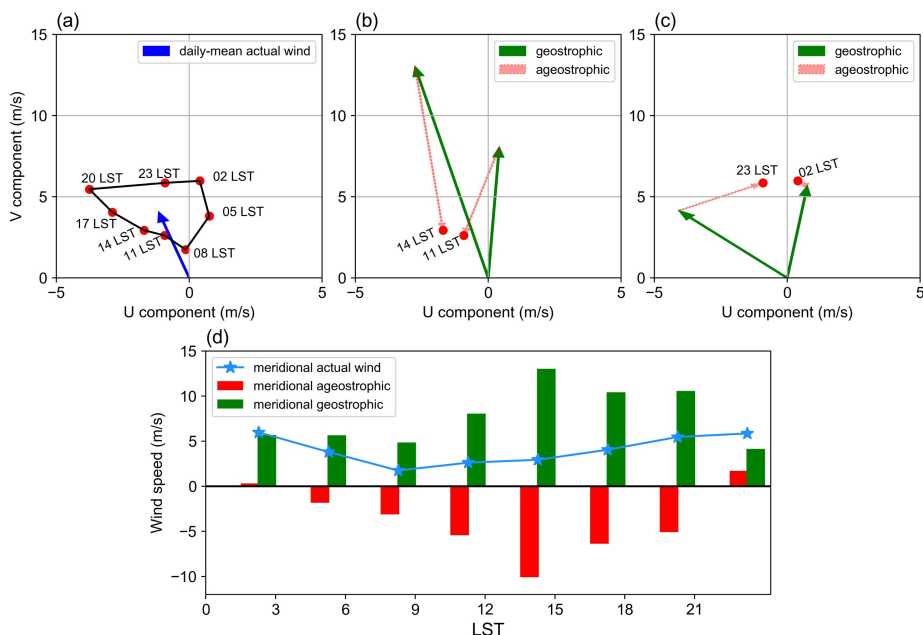
315 To explain the nighttime enhancement of S-LLJ, we analyzed the wind vectors using inertial oscillation theory. To  
316 show more significant diurnal variation, all the time points, including the LLJs that did not occur, were considered.  
317 Figure 10a is the hodograph of jet-core winds at point-a near the Great Plains, and their temporal mean is computed  
318 at 3-hourly intervals in summer. It is noted here that the “jet-core” means the position where LLJ occurs the most  
319 frequently on the cross-section. Compared with the mean actual wind (blue arrow), the deviation at each local time  
320 shows a clear clockwise rotation. The wind speed begins increasing after 17 LST. Nevertheless, the analysis for Figure  
321 9 indicates the sloping heating effect, meaning that the geostrophic wind is not fixed.

322 Thus, to obtain the ageostrophic winds, we computed the geostrophic components by pressure gradient and subtracted  
323 them from the actual airflow. According to the aforementioned definition of geostrophic wind,  $u_g$  and  $v_g$  are



324 calculated by the horizontal pressure gradient  $\frac{\partial P}{\partial y}$  and  $\frac{\partial P}{\partial x}$ , respectively. By choosing four grids surrounding point-a,  
325 we first interpolated the pressure value to the same level as the LLJ core height. Then, we adopted the central difference  
326 equation  $\frac{\Delta P}{\Delta x} = \frac{P_{i+1} - P_{i-1}}{x_{i+1} - x_{i-1}}$  or  $\frac{\Delta P}{\Delta y} = \frac{P_{i+1} - P_{i-1}}{y_{i+1} - y_{i-1}}$  to obtain the pressure gradients at point-a.

327 Figures 10b and 10c display geostrophic wind vectors (green arrows) and ageostrophic vectors (pink) at noon and  
328 midnight. The southerly geostrophic flows are much stronger in the afternoon (10b) than at midnight. The ageostrophic  
329 winds flow mostly in the opposite direction, limiting the actual wind speed. At night (10c), the geostrophic wind  
330 direction rotates clockwise from that of the afternoon as the pressure gradient changes. Considering the relative  
331 positions of green and pink vectors at 23 LST and 01 LST, ageostrophic flow has rotated roughly 150 degrees to  
332 enhance the geostrophic winds, thereby creating a super-geostrophic state. Although the inertial oscillation theory can  
333 help explain some aspects of wind behavior, the real situation is more complex than initially thought. Figures 10b and  
334 10c indicate that by 02 LST, the wind is almost entirely geostrophic with only negligible ageostrophic perturbations.  
335 This suggests that the diurnal changes in the geostrophic wind and pressure gradient may provide a complicating  
336 background that prevents the inertial oscillation theory from fully prevailing. While the inertial oscillation theory can  
337 provide valuable insights, it should not be relied upon as the sole explanation for LLJs at the Great Plains. Instead, a  
338 more comprehensive understanding of atmospheric dynamics is necessary to fully comprehend the behavior of the  
339 wind, particularly when dealing with diurnally changing conditions. Figure 10d compares different meridional wind  
340 components' amplitudes. The geostrophic wind contributes significantly to the southerly wind during the day, peaking  
341 at 14 LST (green bars). The northerly ageostrophic wind (red bars) is highest during the day, indicating the strongest  
342 negative impact from friction. The meridional ageostrophic component decreases and eventually reverses at 23 LST,  
343 showing a process from sub- to super-geostrophic status. In summary, the thermodynamic circulation near the slopes  
344 of the Great Plains contributes to the strong southerly airflow, while the inertial oscillation plays a critical role in  
345 forming the nocturnal southerly LLJ.



346  
 347 **Figure 10. (a) Hodograph of jet-core winds for the Great Plains S-LLJ every 3 hours over the whole JJA (red dots – solid**  
 348 **line) and the daily averaged actual wind velocity (blue vector); vectors of mean jet-core geostrophic winds (solid green) and**  
 349 **ageostrophic winds (dashed red) at (b) 11/14 LST and (c) 23/02 LST; (d) diurnal cycles of meridional components of actual**  
 350 **(blue line), geostrophic (green bars), and ageostrophic winds (red bars).**

351

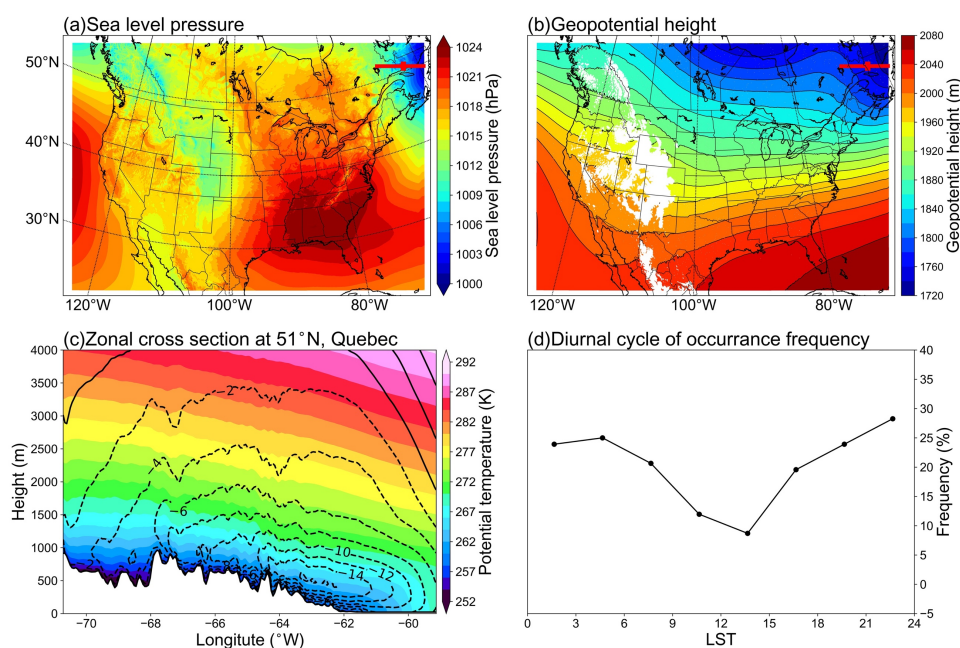
#### 352 4.2 Quebec N-LLJ

353 Similarly, for the Quebec N-LLJ that is typically observed in winter, we selected all the LLJ cases at point-b (see the  
 354 position in Figure 1) in DJF to generate the background circulation pattern. The background large-scale circulations  
 355 indicate that the northeastern coast of Canada lies to the west of a strong surface low-pressure system (Figure 11a),  
 356 while in the lower troposphere, a ridge on the east side of Hudson Bay occupies the Labrador Plateau (Figure 11b).  
 357 This combination brings the northerly momentum to the downstream eastern coast. In fact, the background circulation  
 358 is consistent with the shallow baroclinic structure of Quebec N-LLJ in winter, that is, the thermal difference between  
 359 warm sea and cold land. The cross-section in Figure 11c shows the thermodynamic structure of this N-LLJ: A well-  
 360 defined low-level jet core is located above land and close to the coastline (approximately 63°W). With a maximum  
 361 wind speed of more than 16 m s<sup>-1</sup> and a height of about 400 m, the jet core is located above the mixed layer under the  
 362 warm air covering and on the land side. Notably, the steep isentropic lines slope towards the ocean and finally sink at





363 the position of 60°W. In addition, the diurnal cycle of frequency (Figure 11d) shows that the diurnal signal and peak  
364 frequency of Quebec N-LLJ are much weaker than the Great Plains S-LLJ, becoming weakest at noon and peaking at  
365 midnight, which is consistent with the results reported in Section 3. This diurnal variation can be explained by the  
366 baroclinicity near this region: At night in winter, the land temperature drops faster than the ocean temperature due to  
367 radiative cooling, enhancing the land-sea contrast and thereby the thermal wind above. The gentle slope on the east of  
368 the Labrador Plateau could generate the slope heating effect in the daytime. In this way, the related temperature  
369 gradient from east to west offsets the land-sea thermal difference.



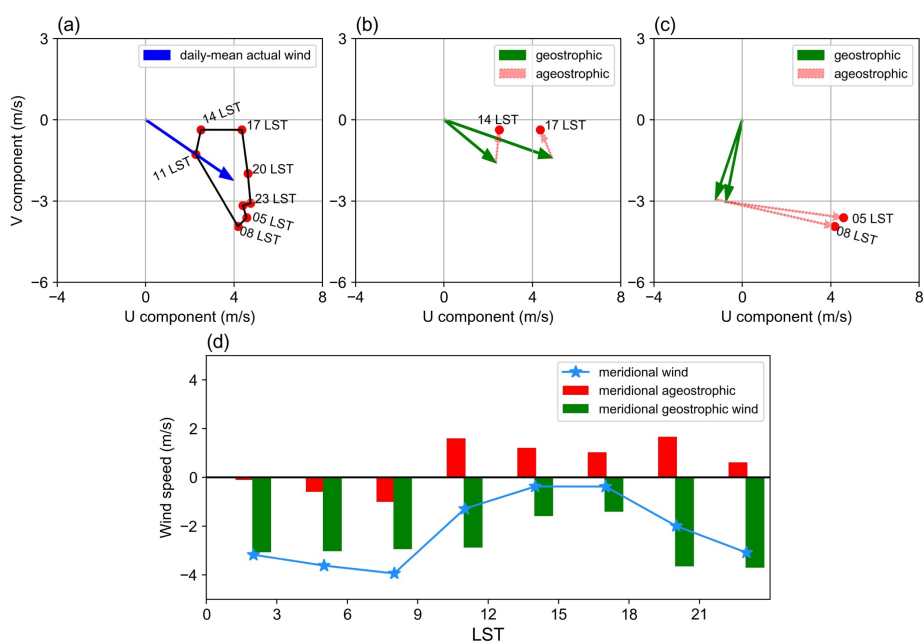
370  
371 **Figure 11. Same as Figure 9 but for Quebec N-LLJs in winter (DJF).**

372 As for the impact of inertial oscillation on the Quebec N-LLJ, the hodograph of averaged 3-hourly winds extracted at  
373 point-b (Figure 12a) also illustrates a clear clockwise rotation of wind deviations compared with the daily mean (blue  
374 arrow). Figure 12b and 12c show that the geostrophic and ageostrophic wind vectors contribute to the diurnal cycle in  
375 the afternoon and morning, respectively. Even though the direction of geostrophic wind changes significantly, the  
376 relative angles between ageostrophic and geostrophic arrows indicate that the ageostrophic flow rotates clockwise.



377 The geostrophic wind is weakened by ageostrophic wind in the afternoon (Figure 12b), whereas the supergeostrophic  
378 state is generated in the morning (Figure 12c).

379 Focusing only on the meridional amplitudes validates this characteristic. In Figure 12d, the blue line that represents  
380 the mean actual meridional wind has the same diurnal trend as the frequency variation in Figure 11d. The northerly  
381 wind is weakest in the afternoon, peaking at night and in the early morning. Similarly, the variation of meridional  
382 geostrophic flow has a consistent phase with the actual meridional wind, which is explained by the baroclinic structure  
383 near the Quebec coast mentioned above. The meridional ageostrophic wind in this region also promotes the formation  
384 of N-LLJ. The ageostrophic wind drags the geostrophic component in the afternoon, before reversing to a consistent  
385 direction with the northerly geostrophic flow at night and in the morning. This trend is also the result of decreasing  
386 friction after sunset. Therefore, the evolution of Quebec N-LLJ derives from both inertial oscillation and land-sea  
387 thermal contrast in winter.



388  
389 **Figure 12. Same as Figure 10 but for Quebec N-LLJs in winter (DJF).**

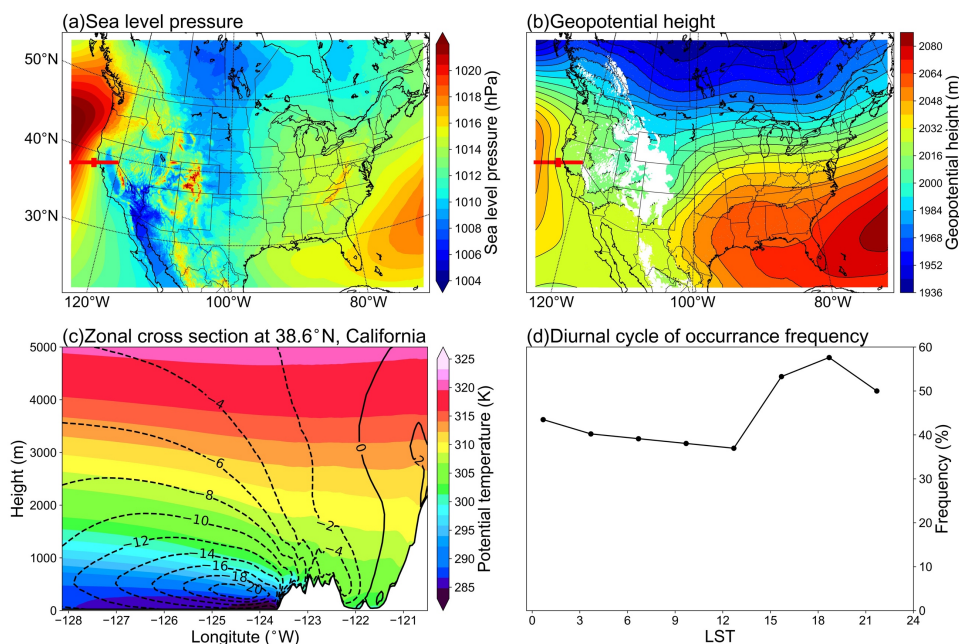
390

### 391 **4.3 California coastal N-LLJ**





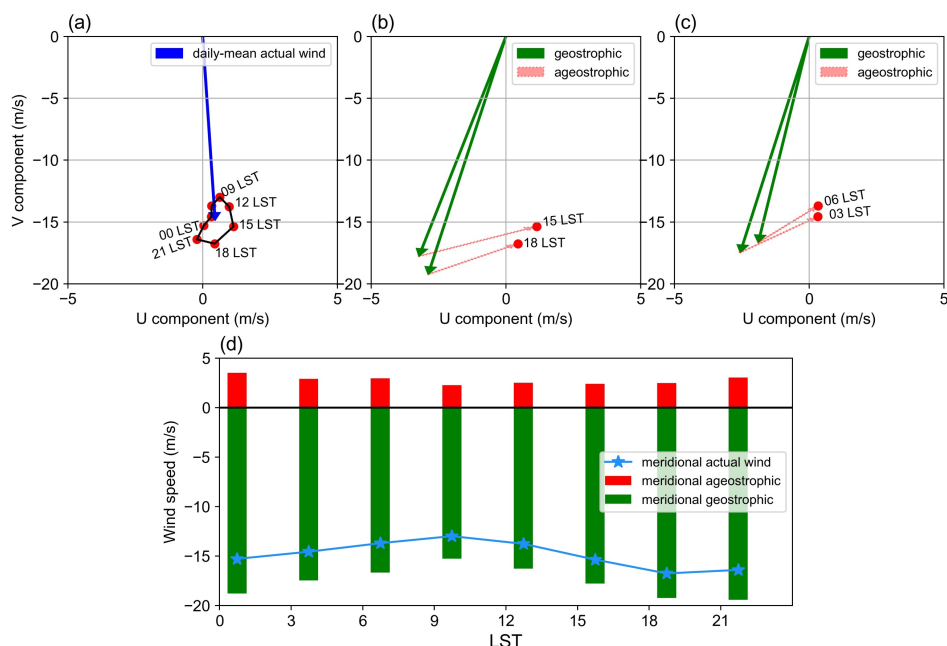
392 The California coastal N-LLJ is similar to the one in Quebec, but it occurs more often in summer afternoons or  
393 evenings over the ocean. Figure 13a shows that a relatively strong high-pressure system is located on the east coast of  
394 the Pacific Ocean, trending NE-SW, although half of the structure is beyond the boundary of the domain. On the 800  
395 hPa isobaric surface in Figure 13b, there is also an anticyclone system in the same location, whose eastern contour is  
396 roughly parallel to the coastline, guiding the airflow to the south. Therefore, this pair is also forced by the thermal  
397 difference between land and sea, but contrary to the LLJ in Quebec, in summer, when the California LLJ occurs  
398 frequently, it has the characteristics of the cool sea-hot land. Figure 13b also shows that the isobars near Cape  
399 Mendocino are relatively strong, making the ridge of high pressure extend northeastward of the Cape. This extension  
400 is generally believed to occur due to pressure perturbation caused when northerly winds converge at this position after  
401 being obstructed (Rahn and Parish, 2007). Regarding the cross-section structure shown in Figure 13c, the jet core is  
402 located at steep isentropic lines above the ocean at a height of 500 m. On the coast of California, the LLJ is close to  
403 the mountains. Compared with the Quebec LLJ, California's maximum central wind speed exceeds 20 m s<sup>-1</sup>. Based  
404 on baroclinicity, the isentropic lines slope towards the continent and finally sink near the coastline. The core wind  
405 speed in California's coastal LLJ may be higher than that of Quebec's LLJ because the land-sea contrast is more  
406 significant in summer than in winter and the formed sea breeze front generates flow convergence under the blockage  
407 caused by the west coast mountains. In contrast, the east coast of Quebec is relatively gentle, which may account for  
408 its lower wind speed. Because California's LLJ occurs frequently (13d), the diurnal signal is weak compared, for  
409 example, to the signal in the Great Plain S-LLJ. As well, the California signal stays at frequency of over 35%.  
410 California's LLJ occurs most frequently at around 18 LST and starts to decline after sunset, which is generally  
411 consistent with the coastal baroclinicity.



412

413 **Figure 13. Same as Figure 9 but for California Coastal S-LLJ in summer (JJA).**

414 The wind deviations for California's N-LLJ shown in the hodograph (Figure 14a) still have a clockwise rotation in 24  
415 hours. However, compared with the magnitude of the daily mean jet-core wind, this diurnal cycle is not quite as  
416 obvious as the cycle for Quebec and Great Plain LLJs, but it is similar to the frequency cycle shown in Figure 13d. In  
417 comparison between geostrophic and ageostrophic winds (Figure 14b and 14c), during the afternoon (15 and 18 LST),  
418 the amplitude of geostrophic wind is the largest, and the ageostrophic flow diminishes the geostrophic wind. However,  
419 in the morning 12 hours later, the relative angle between ageostrophic and geostrophic vectors does not change,  
420 meaning that the ageostrophic wind is still weakening the geostrophic wind and that there is no rotation of the  
421 ageostrophic wind, as Blackadar inertial oscillation theory describes. Figure 14d helps to explain the change in  
422 meridional winds. Looking at the magnitudes of ageostrophic winds, one can see that all are weak and southerly and  
423 that they do not exhibit a significant diurnal signal. Furthermore, the change of geostrophic wind is highly consistent  
424 with the trend of the actual meridional wind. Thus, the N-LLJ in California can be considered mostly as geostrophic  
425 and the diurnal variation as being related to the change in geostrophic winds.



426

427 **Figure 14.** Same as Figure 10 but for California Coastal S-LLJ in summer (JJA).

428

## 429 **5 Discussion and conclusion**

430 This study applied a convection-permitting WRF model to generate the climatology of LLJs in North America. The  
431 previous research for LLJs mainly focused on observation data, which have no fine coverage in temporal or spatial  
432 resolution. The studies using in-situ observations may ignore some important features. Despite their better coverage,  
433 reanalysis datasets usually have a coarse spatial resolution, especially in the vertical direction, and can introduce large  
434 inaccuracies in the identification of LLJs. In addition, the application of general numerical modeling cannot avoid the  
435 uncertainty caused by parameterizing small-scale physical processes. In contrast, high-resolution convection-  
436 permitting climate simulations can provide more reliable and accurate descriptions of LLJs, especially for areas with  
437 complex geographic conditions or regions that lack soundings. Previous studies using high-resolution models  
438 conducted case analyses only of LLJs in a specific region (Aird et al., 2022). By expanding the target domain to the  
439 whole of North America and revealing the climatological characteristics of LLJs in different regions and scales, this  
440 paper provides an accurate reference for future research on LLJ-related processes in North America.

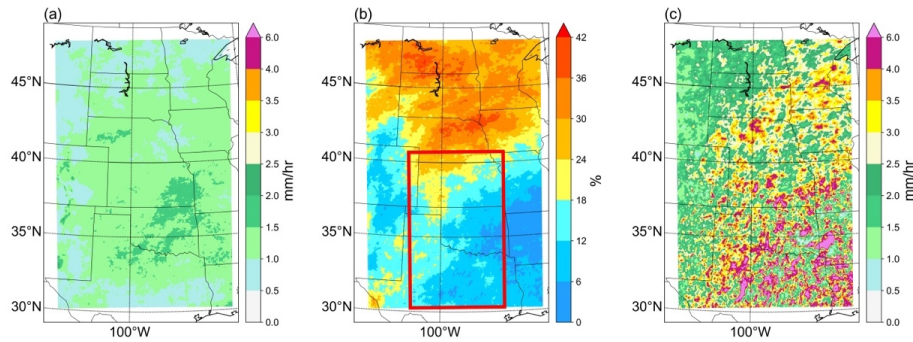


441 The convection-permitting WRF model is able to recapture some LLJs that have been previously studied, such as the  
442 Great Plain S-LLJ and the California coastal N-LLJ in the eastern Pacific Ocean and has obtained relatively consistent  
443 results. The results indicate that the S-LLJ in the central US Plain is the most frequent and active in warm seasons and  
444 that three critical high-frequency centers occur in summer: the northeast Mexico-Texas border, west-central Texas,  
445 and western Oklahoma to southern Kansas. This last result is consistent with the climatology generated by Doubler et  
446 al. (2015) using the NARR reanalysis data, but the patterns here are more representative of the topographic features  
447 in central and southern Texas. In addition, compared with the 40-year rawinsonde climatology in the central US by  
448 Walters et al. (2008), our study reveals that the S-LLJ frequency range of these three centers in the central US in  
449 summer is 25%-30%, which is slightly lower than the 35% reported in the 2008 study. However, given the  
450 underestimated frequencies of 15%-20% in NARR climatology, there is an advantage of using high-resolution  
451 simulations in the vertical direction.

452 Convection-permitting simulations can also capture the LLJs that were barely detected previously. The winter N-LLJs  
453 over the eastern Rocky Mountains described in this paper are generally distributed over the central US from the  
454 Dakotas to Oklahoma with a low frequency (>10%) and over several sporadic small areas with a high frequency  
455 (>20%) along the boundary of the Rockies. The main seasonal/diurnal variations identified in this study agree with  
456 those seen using rawinsonde data (Walters et al., 2008) and NARR reanalysis (Douber et al., 2015). But the frequency  
457 of the LLJ occurrence over Nebraska-Kansas was underestimated in both convection-permitting simulations (~10%)  
458 and NARR (~7%), while high-frequency hot spots from Alberta to Colorado were not detected in either of the above-  
459 mentioned studies, probably because measurements are lacking in these regions. The high-resolution simulation also  
460 detected LLJs on which researchers have hardly focused: N-LLJs near the eastern Quebec coast and in the  
461 Appalachians Mountains, as well as an S-LLJ over the British Columbia coast. In the work of Douber et al. (2015),  
462 these LLJs were shown in the climatology patterns, but the 4-km WRF simulation offered more detailed descriptions  
463 of their locations. For example, this study found that the Appalachian N-LLJ extends from Georgia to the northwestern  
464 Atlantic, especially on summer nights (03 UTC – 06 UTC), while NARR only captured LLJ occurrences over the  
465 middle coast of the Atlantic. The maximum frequency (7-10%) detected in the NARR study is also less than what is  
466 illustrated here. As for the Quebec N-LLJ, the 4-km WRF revealed that it mostly occurs onshore near the coast with  
467 a frequency of over 25% in winter, but NARR only provided a coarse occurrence distribution over northeastern Canada.

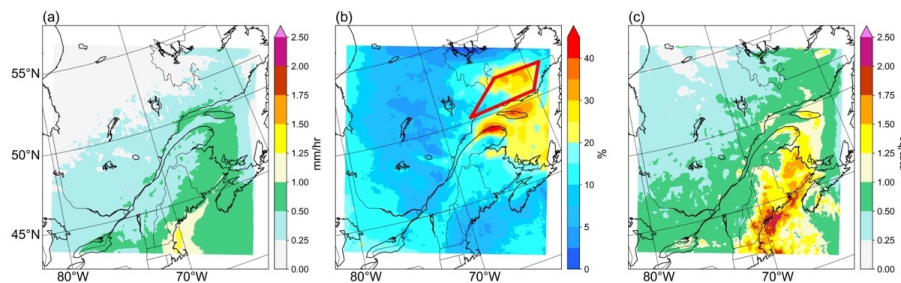


468 To investigate the significance of LLJs in different regions, Figures 15 and 16 demonstrate the impact of the Great  
469 Plains S-LLJ and Quebec N-LLJ, respectively, on downstream extreme precipitation during their active seasons.  
470 Figure 15a illustrates the 90th percentile of summer precipitation in the central United States, indicating that 90% of  
471 the precipitation in most areas falls within the range of 1.0-2.0 mm/hour. However, Figure 15b shows the ratio of  
472 strong events related to LLJs (counted if the precipitation is > 90th percentile when a LLJ occurs) to all strong events,  
473 with the red outline on the map indicating the approximate location of the low-level jet stream. It is evident that in the  
474 lower reaches of the S-LLJ in the Great Plain, particularly in the north-central United States, nearly 50% of the heavy  
475 precipitation events are associated with the flourishing low-level jet stream. Furthermore, Figure 15c displays the  
476 average precipitation of all LLJ-related strong events. Compared with Figure 15a, some areas of Nebraska and  
477 Minnesota experience rainfall of up to 6mm/hour. These findings highlight the significant role played by LLJ in  
478 modulating summer precipitation. Similarly, for the Quebec N-LLJ in winter (Fig. 16), it contributes more than 25%  
479 of the strong events of precipitation in the Gulf of St. Lawrence during winter (Fig. 16b). Figure 16c further reveals  
480 that, in comparison to the 90th percentile rainfall, the extreme precipitation from Quebec to Maine is approximately  
481 1mm/hr higher. Particularly during the cold season when a substantial portion of precipitation is snow, the N-LLJs  
482 can also be seen as the factors of snowstorms in this region. In summary, research on the importance of LLJs includes  
483 not only the field of extreme precipitation, but also local wind energy production, air pollution dispersion, wildfires,  
484 etc. (Jain & Flannigan 2021, Lin et al. 2022, Weide Luiz & Fiedler 2022). There is no doubt that the high-resolution  
485 regional climate model presented in this paper provides ample coverage and details about LLJs in North America, to  
486 support analysis in these fields, particularly at the national level. With a grid spacing as small as 4 km, researchers can  
487 even employ the wind profiles from model output to investigate small-scale areas, such as wind farms or wildfire  
488 ignition sites.



489

490 **Figure 15. (a) 90th percentile of summer precipitation rate over Central US; (b) The ratio of LLJ-related strong rainfall**  
491 **events to all strong events, the red outline represents the location of Great Plain S-LLJ; (c) Averaged precipitation rate of**  
492 **LLJ-related strong events.**



493

494 **Figure 16. (a) 90th percentile of winter precipitation rate over Southeastern Canada; (b) The ratio of LLJ-related strong**  
495 **rainfall events to all strong events, the red outline represents the location of Quebec N-LLJ; (c) Averaged precipitation rate**  
496 **of LLJ-related strong events.**

497 Based on the inertial oscillation theory (Blackadar, 1957) and the baroclinic theory near complex terrain (Holton,  
498 1967), this paper also analyzed the background and formation mechanisms of three LLJs: the Great Plain S-LLJ,  
499 Quebec N-LLJ, and California coastal N-LLJ. Generally, all these LLJs are impacted by the thermodynamic  
500 circulations generated near their topography. The Great Plain S-LLJ is affected by slope heating, and the LLJs over  
501 Quebec and California are associated with the sea-land contrast. When the geostrophic and ageostrophic components  
502 of the LLJs are compared, results show that the inertial oscillation better explains the night enhancement of the Great  
503 Plains S-LLJ and that the diurnal feature of the Quebec N-LLJ is influenced by the combination of the Holton and  
504 Blackadar theories. As for the California coastal N-LLJ, no supergeostrophic state is found, making coastal  
505 baroclinicity variation a dominant factor for this LLJ's evolution the geostrophic wind changes.



506 The LLJs climatology introduced in this research adds to the existing knowledge of characteristics of the low-level  
507 wind maxima in North America, thus helping researchers obtain more reliable references about LLJs in this domain.  
508 Meanwhile, with the high-resolution features, it can provide more robust explanations for other interdisciplinary fields.  
509 The research also advances knowledge about the formation of three dominant LLJs. Although the 13-year simulation  
510 is likely too short to provide an ideal long-term climatic analysis, it is a less expensive option for finer numerical  
511 modeling in large domains. But it is also believed that with the advancement of technology, there will be longer high-  
512 resolution simulations in the future. Future work will address the features and formation mechanisms of the small-  
513 scale low-level wind maxima that have yet to be investigated.



514 **Acknowledgments**

515 All authors thank the support of the Global Water Futures Program by the Canada First Research Excellence and the  
516 NSERC Discovery Grant.

517

518 **Data Availability Statement**

519 The WRF simulation over CONUS can be accessed at Research Data Archive of NCAR  
520 <https://rda.ucar.edu/datasets/ds612.0/>.

521

522 **Author contribution**

523 Xiao Ma: Conceptualization; data curation; formal analysis; investigation; methodology; visualization; writing-  
524 original draft.

525 Yanping Li: Conceptualization; funding acquisition; investigation; methodology; project administration; supervision;  
526 validation; writing-review and editing.

527 Zhenhua Li: Data curation; methodology; validation; visualization; writing-review and editing.

528 Fei Huo: Data curation; methodology; validation; visualization; writing-review and editing.

529

530 **Competing interests**

531 All authors disclosed no relevant relationships.

532



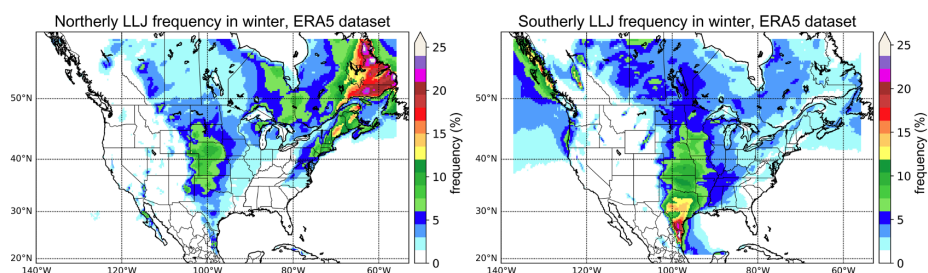


533 **Appendix**

534 **Winter LLJs captured by ERA5 Dataset**

535 The convection-permitting WRF simulation exhibited excellent performance in investigating well-known LLJ systems,  
536 such as the California coastal N-LLJ and the Great Plains S-LLJ. Moreover, this appendix validates WRF-simulated  
537 significant winter jet systems over North America using the ERA5 reanalysis dataset. ERA5 is a global atmospheric  
538 reanalysis dataset produced by the European Centre for Medium-Range Weather Forecasts (ECMWF). It provides  
539 hourly data on a horizontal grid space of approximately 31 km, and the time range covers from 1979 till the present.  
540 ERA5 data is widely used in climate research, weather forecasting, and various applications that require high-quality  
541 atmospheric data.

542 The validation period is the same as the WRF simulation (2000-2013). From the Figure A1 below, it is evident that  
543 during winter, a greater number of significant N-LLJ systems in the North American continent are mostly concentrated  
544 in eastern Canada. In most parts of Newfoundland and southeastern Quebec, the occurrence frequency of N-LLJs  
545 exceeds 15%, and the maximum can even surpass 25%. However, in the WRF simulation (Figure 3d), the model can  
546 only capture N-LLJs on the north bank of the St. Lawrence River due to the northern boundary of the study domain  
547 overlapping with the Quebec border. In comparison, the WRF-simulated frequency of N-LLJs in southeastern Quebec  
548 essentially exceeds 25%, overestimated by about 5% compared to the ERA5 reanalysis. Additionally, it is worth noting  
549 that the N-LLJs along the downstream of Rockies are also identified in the ERA5 dataset. The areas where the  
550 frequency exceeds 5% are mainly distributed from Alberta to northern Texas, consistent with the findings in Section  
551 3.2.1. Moreover, the high-value center (>10%) is located in central Kansas. In terms of the differences between the  
552 two datasets, the results of the WRF simulation match more geographical features and reveal scattered high-value  
553 spots (>15%) in some regions with special terrains (see Figure 3d). Furthermore, the winter Great Plains S-LLJs in  
554 ERA5 reanalysis exhibit similar features, with frequencies ranging from around 15% to 20% in southern Texas. In  
555 summary, the WRF model can accurately capture the features of winter LLJ systems, which are validated by the ERA5  
556 reanalysis dataset over northern America. Even though the frequency of LLJs occurrence is overestimated, the  
557 convection-permitting WRF simulation can provide detailed descriptions of LLJs near complex terrains.



558

559 **Figure A1. Winter occurrence frequency of N-LLJs (left) and S-LLJs (right).**

560

561

562

563 **Data Availability Statement**

564 The ERA5 dataset is available on the Copernicus Climate Change Service Information website.

565 <https://cds.climate.copernicus.eu/#!/home>

566

567



568 **References**

- 569 Aird, J. A., Barthelmie, R. J., Shepherd, T. J. and Pryor, S. C.: Occurrence of Low-Level Jets over the Eastern U.S.  
570 Coastal Zone at Heights Relevant to Wind Energy, *Energies*, 15(2), 445, doi:10.3390/en15020445, 2022.
- 571 Blackadar, A. K.: Boundary Layer Wind Maxima and Their Significance for the Growth of Nocturnal Inversions,  
572 *Bulletin of the American Meteorological Society*, 38(5), 283–290, doi:10.1175/1520-0477-38.5.283, 1957.
- 573 Bonner, W. D.: CLIMATOLOGY OF THE LOW LEVEL JET, *Monthly Weather Review*, 96(12), 833–850,  
574 doi:10.1175/1520-0493(1968)096<0833:cotllj>2.0.co;2, 1968.
- 575 Chen, G. T.-J., Wang, C.-C. and Lin, D. T.-W.: Characteristics of Low-Level Jets over Northern Taiwan in Mei-Yu  
576 Season and Their Relationship to Heavy Rain Events, *Monthly Weather Review*, 133(1), 20–43, doi:10.1175/mwr-  
577 2813.1, 2005.
- 578 Doubler, D. L., Winkler, J. A., Bian, X., Walters, C. K. and Zhong, S.: An NARR-Derived Climatology of Southerly  
579 and Northerly Low-Level Jets over North America and Coastal Environs, *Journal of Applied Meteorology and*  
580 *Climatology*, 54(7), 1596–1619, doi:10.1175/jamc-d-14-0311.1, 2015.
- 581 Du, Y. and Chen, G.: Heavy Rainfall Associated with Double Low-Level Jets over Southern China. Part II: Convection  
582 Initiation, *Monthly Weather Review*, 147(2), 543–565, doi:10.1175/mwr-d-18-0102.1, 2019.
- 583 Frisch, A. S., Orr, B. W. and Martner, B. E.: Doppler Radar Observations of the Development of a Boundary-Layer  
584 Nocturnal Jet, *Monthly Weather Review*, 120(1), 3–16, doi:10.1175/1520-  
585 0493(1992)120<0003:drootd>2.0.co;2, 1992.
- 586 Fu, P., Zhu, K., Zhao, K., Zhou, B. and Xue, M.: Role of the nocturnal low-level jet in the formation of the morning  
587 precipitation peak over the Dabie Mountains, *Advances in Atmospheric Sciences*, 36(1), 15–28, doi:10.1007/s00376-  
588 018-8095-5, 2018.
- 589 Gadde, S. N. and Stevens, R. J. A. M.: Effect of low-level jet height on wind farm performance, *Journal of Renewable*  
590 *and Sustainable Energy*, 13(1), 013305, doi:10.1063/5.0026232, 2021.



- 591 Hodges, D. and Pu, Z.: Characteristics and Variations of Low-Level Jets and Environmental Factors Associated with  
592 Summer Precipitation Extremes over the Great Plains, *Journal of Climate*, 32(16), 5123–5144, doi:10.1175/jcli-d-18-  
593 0553.1, 2019.
- 594 Holton, J. R.: The diurnal boundary layer wind oscillation above sloping terrain, *Tellus*, 19(2), 199–205,  
595 doi:10.1111/j.2153-3490.1967.tb01473.x, 1967.
- 596 Hong, S.-Y., Noh, Y. and Dudhia, J.: A New Vertical Diffusion Package with an Explicit Treatment of Entrainment  
597 Processes, *Monthly Weather Review*, 134(9), 2318–2341, doi:10.1175/mwr3199.1, 2006.
- 598 Hu, X.-M., Klein, P. M., Xue, M., Lundquist, J. K., Zhang, F. and Qi, Y.: Impact of Low-Level Jets on the Nocturnal  
599 Urban Heat Island Intensity in Oklahoma City, *Journal of Applied Meteorology and Climatology*, 52(8), 1779–1802,  
600 doi:10.1175/jamc-d-12-0256.1, 2013.
- 601 Iacono, M. J., Delamere, J. S., Mlawer, E. J., Shephard, M. W., Clough, S. A. and Collins, W. D.: Radiative forcing  
602 by long-lived greenhouse gases: Calculations with the AER radiative transfer models, *Journal of Geophysical*  
603 *Research*, 113(D13), doi:10.1029/2008jd009944, 2008.
- 604 Jain, P. and Flannigan, M.: The relationship between the Polar Jet Stream and extreme wildfire events in North  
605 America, *Journal of Climate*, 1–59, doi:10.1175/jcli-d-20-0863.1, 2021.
- 606 Jiménez-Sánchez, G., Markowski, P. M., Jewtoukoff, V., Young, G. S. and Stensrud, D. J.: The Orinoco Low-Level  
607 Jet: An Investigation of Its Characteristics and Evolution Using the WRF Model, *Journal of Geophysical Research:*  
608 *Atmospheres*, 124(20), 10696–10711, doi:10.1029/2019jd030934, 2019.
- 609 Kurkute, S., Li, Z., Li, Y. and Huo, F.: Assessment and projection of the water budget over Western Canada using  
610 convection-permitting weather research and forecasting simulations, *Hydrology and Earth System Sciences*, 24(7),  
611 3677–3697, doi:10.5194/hess-24-3677-2020, 2020.



- 612 Li, Y., Li, Z., Zhang, Z., Chen, L., Kurkute, S., Scaff, L. and Pan, X.: High-resolution regional climate modeling and  
613 projection over Western Canada using a weather research forecasting model with a pseudo-global warming approach,  
614 Hydrology and Earth System Sciences, 23(11), 4635–4659, doi:10.5194/hess-23-4635-2019, 2019.
- 615 Lin, Y., Wang, C., Yan, J., Li, J. and He, S.: Observation and simulation of low-level jet impacts on 3D urban heat  
616 islands in Beijing: A case study, Journal of the Atmospheric Sciences, 79(8), 2059–2073, doi:10.1175/jas-d-21-0245.1,  
617 2022.
- 618 Liu, C., Ikeda, K., Rasmussen, R., Barlage, M., Newman, A. J., Prein, A. F., Chen, F., Chen, L., Clark, M., Dai, A.,  
619 Dudhia, J., Eidhammer, T., Gochis, D., Gutmann, E., Kurkute, S., Li, Y., Thompson, G. and Yates, D.: Continental-  
620 scale convection-permitting modeling of the current and future climate of North America, Climate Dynamics, 49(1–  
621 2), 71–95, doi:10.1007/s00382-016-3327-9, 2016.
- 622 Ma, X., Li, Y. and Li, Z.: The projection of Canadian wind energy potential in future scenarios using a convection-  
623 permitting regional climate model, Energy Reports, 8, 7176–7187, doi:10.1016/j.egy.2022.05.122, 2022.
- 624 Miao, Y., Guo, J., Liu, S., Wei, W., Zhang, G., Lin, Y., Zhai, P., Zhai, P., Lin, Y., Zhang, G., Wei, W., Liu, S., Guo,  
625 J. and Miao, Y.: The Climatology of Low-Level Jet in Beijing and Guangzhou, China, Journal of Geophysical  
626 Research: Atmosphere, 123(5), 2816–2830, doi:10.1002/2017jd027321, 2018.
- 627 Mitchell, M. J., Arritt, R. W. and Labas, K.: A Climatology of the Warm Season Great Plains Low-Level Jet Using  
628 Wind Profiler Observations, Weather and Forecasting, 10(3), 576–591, doi:10.1175/1520-  
629 0434(1995)010<0576:acotws>2.0.co;2, 1995.
- 630 Montini, T. L., Jones, C. and Carvalho, L. M. V.: The South American Low-Level Jet: A New Climatology, Variability,  
631 and Changes, Journal of Geophysical Research: Atmospheres, 124(3), 1200–1218, doi:10.1029/2018jd029634, 2019.
- 632 Munday, C., Washington, R. and Hart, N.: African Low-Level Jets and Their Importance for Water Vapor Transport  
633 and Rainfall, Geophysical Research Letters, 48(1), doi:10.1029/2020gl090999, 2021.



- 634 Niu, G.-Y., Yang, Z.-L., Mitchell, K. E., Chen, F., Ek, M. B., Barlage, M., Kumar, A., Manning, K., Niyogi, D.,  
635 Rosero, E., Tewari, M. and Xia, Y.: The community Noah land surface model with multiparameterization options  
636 (Noah-MP): 1. Model description and evaluation with local-scale measurements, *Journal of Geophysical Research*,  
637 116(D12), doi:10.1029/2010jd015139, 2011.
- 638 Parish, T. R.: Forcing of the Summertime Low-Level Jet along the California Coast, *Journal of Applied Meteorology*,  
639 39(12), 2421–2433, doi:10.1175/1520-0450(2000)039<2421:fotsll>2.0.co;2, 2000.
- 640 Rahn, D. A. and Parish, T. R.: Diagnosis of the Forcing and Structure of the Coastal Jet near Cape Mendocino Using  
641 In Situ Observations and Numerical Simulations, *Journal of Applied Meteorology and Climatology*, 46(9), 1455–1468,  
642 doi:10.1175/jam2546.1, 2007.
- 643 Rife, D. L., Pinto, J. O., Monaghan, A. J., Davis, C. A. and Hannan, J. R.: Global Distribution and Characteristics of  
644 Diurnally Varying Low-Level Jets, *Journal of Climate*, 23(19), 5041–5064, doi:10.1175/2010jcli3514.1, 2010.
- 645 Saulo, C., Ruiz, J. and Skabar, Y. G.: Synergism between the Low-Level Jet and Organized Convection at Its Exit  
646 Region, *Monthly Weather Review*, 135(4), 1310–1326, doi:10.1175/mwr3317.1, 2007.
- 647 Shapiro, A., Fedorovich, E. and Rahimi, S.: A unified theory for the Great Plains Nocturnal low-level jet, *Journal of*  
648 *the Atmospheric Sciences*, 73(8), 3037–3057, doi:10.1175/jas-d-15-0307.1, 2016.
- 649 Smith, E. N., Gebauer, J. G., Klein, P. M., Fedorovich, E. and Gibbs, J. A.: The Great Plains Low-Level Jet during  
650 PECAN: Observed and Simulated Characteristics, *Monthly Weather Review*, 147(6), 1845–1869, doi:10.1175/mwr-  
651 d-18-0293.1, 2019.
- 652 Stensrud, D. J.: Importance of Low-Level Jets to Climate: A Review, *Journal of Climate*, 9(8), 1698–1711,  
653 doi:10.1175/1520-0442(1996)009<1698:iolljt>2.0.co;2, 1996.
- 654 Sullivan, J. T., Rabenhorst, S. D., Dreessen, J., McGee, T. J., Delgado, R., Twigg, L. and Sumnicht, G.: Lidar  
655 observations revealing transport of O<sub>3</sub> in the presence of a nocturnal low-level jet: Regional implications for “next-  
656 day” pollution, *Atmospheric Environment*, 158, 160–171, doi:10.1016/j.atmosenv.2017.03.039, 2017.



- 657 Tang, Y., Winkler, J., Zhong, S., Bian, X., Doubler, D., Yu, L. and Walters, C.: Future changes in the climatology of  
658 the Great Plains low-level jet derived from fine resolution multi-model simulations, *Scientific Reports*, 7(1),  
659 doi:10.1038/s41598-017-05135-0, 2017.
- 660 Uccellini, L. W., Petersen, R. A., Kocin, P. J., Brill, K. F. and Tuccillo, J. J.: Synergistic Interactions between an  
661 Upper-Level Jet Streak and Diabatic Processes that Influence the Development of a Low-Level Jet and a Secondary  
662 Coastal Cyclone, *Monthly Weather Review*, 115(10), 2227–2261, doi:10.1175/1520-  
663 0493(1987)115<2227:sibaul>2.0.co;2, 1987.
- 664 Van de Wiel, B. J., Moene, A. F., Steeneveld, G. J., Baas, P., Bosveld, F. C. and Holtslag, A. A.: A conceptual view  
665 on inertial oscillations and nocturnal low-level jets, *Journal of the Atmospheric Sciences*, 67(8), 2679–2689,  
666 doi:10.1175/2010jas3289.1, 2010.
- 667 Walters, C. K. and Winkler, J. A.: Airflow Configurations of Warm Season Southerly Low-Level Wind Maxima in  
668 the Great Plains. Part I: Spatial and Temporal Characteristics and Relationship to Convection, *Weather and*  
669 *Forecasting*, 16(5), 513–530, doi:10.1175/1520-0434(2001)016<0513:acowss>2.0.co;2, 2001.
- 670 Walters, C. K., Winkler, J. A., Shadbolt, R. P., van Ravensway, J. and Bierly, G. D.: A Long-Term Climatology of  
671 Southerly and Northerly Low-Level Jets for the Central United States, *Annals of the Association of American*  
672 *Geographers*, 98(3), 521–552, doi:10.1080/00045600802046387, 2008.
- 673 Weide Luiz, E. and Fiedler, S.: Spatiotemporal observations of nocturnal low-level jets and impacts on wind  
674 power production, *Wind Energy Science*, 7(4), 1575–1591, doi:10.5194/wes-7-1575-2022, 2022.
- 675 Zhang, Y., Xue, M., Zhu, K. and Zhou, B.: What is the main cause of diurnal variation and nocturnal peak of summer  
676 precipitation in Sichuan Basin, China? the key role of boundary layer low-level jet inertial oscillations, *Journal of*  
677 *Geophysical Research: Atmospheres*, 124(5), 2643–2664, doi:10.1029/2018jd029834, 2019.
- 678 Zhong, S., Fast, J. D. and Bian, X.: A Case Study of the Great Plains Low-Level Jet Using Wind Profiler Network  
679 Data and a High-Resolution Mesoscale Model, *Monthly Weather Review*, 124(5), 785–806, doi:10.1175/1520-  
680 0493(1996)124<0785:acsotg>2.0.co;2, 1996.